Ocean Sci., 11, 121–138, 2015
www.ocean-sci.net/11/121/2015/
doi:10.5194/os-11-121-2015

Ocean Science
Open Access

Measuring air–sea gas-exchange velocities in a large-scale annular wind–wave tank

E. Mesarchaki[1], C. Kräuter[2], K. E. Krall[2], M. Bopp[2], F. Helleis[1], J. Williams[1], and B. Jähne[2,3]

[1]Max-Planck-Institut für Chemie (Otto-Hahn-Institut) Hahn-Meitner-Weg 1, 55128 Mainz, Germany
[2]Institut für Umweltphysik Universität Heidelberg, Im Neuenheimer Feld 229, 69120 Heidelberg, Germany
[3]Heidelberg Collaboratory for Image Processing (HCI), Universität Heidelberg, Speyerer Straße 6, 69115 Heidelberg, Germany

Correspondence to: E. Mesarchaki (evridiki.mesarchaki@mpic.de)

Received: 1 May 2014 – Published in Ocean Sci. Discuss.: 23 June 2014
Revised: 28 November 2014 – Accepted: 17 December 2014 – Published: 28 January 2015

Abstract. In this study we present gas-exchange measurements conducted in a large-scale wind–wave tank. Fourteen chemical species spanning a wide range of solubility (dimensionless solubility, $\alpha = 0.4$ to 5470) and diffusivity (Schmidt number in water, $Sc_w = 594$ to 1194) were examined under various turbulent ($u_{10} = 0.73$ to $13.2\,\mathrm{m\,s^{-1}}$) conditions. Additional experiments were performed under different surfactant modulated (two different concentration levels of Triton X-100) surface states. This paper details the complete methodology, experimental procedure and instrumentation used to derive the total transfer velocity for all examined tracers. The results presented here demonstrate the efficacy of the proposed method, and the derived gas-exchange velocities are shown to be comparable to previous investigations. The gas transfer behaviour is exemplified by contrasting two species at the two solubility extremes, namely nitrous oxide (N_2O) and methanol (CH_3OH). Interestingly, a strong transfer velocity reduction (up to a factor of 3) was observed for the relatively insoluble N_2O under a surfactant covered water surface. In contrast, the surfactant effect for CH_3OH, the high solubility tracer, was significantly weaker.

1 Introduction

The world's oceans are key sources and sinks in the global budgets of numerous atmospherically important trace gases, in particular CO_2, N_2O and volatile organic compounds (VOCs) (Field et al., 1998; Williams et al., 2004; Millet et al., 2008, 2010; Carpenter et al., 2012). Gas exchange between the ocean and the atmosphere is therefore a significant conduit within global biogeochemical cycles. Air–sea gas fluxes, provided by either direct flux measurements or accurate gas transfer parameterisations, are a prerequisite for global climate models tasked to deliver accurate future predictions (Pozzer et al., 2006; Saltzman, 2009).

The principles behind gas exchange at the air–sea interface have been reported in detail within previous reviews (Jähne and Haußecker, 1998; Donelan and Wanninkhof, 2002; Wanninkhof et al., 2009; Jähne, 2009; Nightingale, 2009). A simplified conceptual two layer model is generally accepted. The model assumes that close to the interface turbulent motion is suppressed and that the transfer of gases is controlled by molecular motion (expressed by the diffusion coefficient D). This leads to the formation of two mass boundary layers on both sides of the interface. In the upper part of the air-side mass boundary layer, turbulent transport becomes significant. Further away from the interface the significance of the air-side turbulent transport increases. In the water-side, due to lower diffusivities, molecular transport remains the controlling factor of the transfer. Depending on the solubility of the gas in question, its transfer could be restricted by one or both sides of the interface (i.e air-side and water-side controlled).

The transfer velocity, k (in $\mathrm{cm\,h^{-1}}$), of a gas across the surface is defined as the gas flux density, F, divided by the concentration difference, Δc, between air and water (henceforth named k_t expressing the transfer through both boundary layers against the single air and water layer transfer, k_a and k_w, accordingly). Wind-driven turbulence near the water surface

as well as the resultant processes (surface stress and roughness, waves, breaking waves, bubbles, spray, etc.) influences the thickness of the mass boundary layers. Thus, the transfer velocity is related to the degree of turbulence on both sides close to the interface as well as the tracer characteristics, i.e. their solubility and diffusion coefficients (Danckwerts, 1951; Liss and Slater, 1974). Surface films are also known to have a strong influence on the transfer velocity by inhibiting waves and decreasing the near-surface turbulence (e.g Frew et al., 1990; Jähne and Haußecker, 1998; Zappa et al., 2004; Salter et al., 2011). To date, research on surface films (using different film thicknesses and types) and their effect on transfer velocity is only in the very early stages. The impact of wind-driven mechanisms, surface films and diverse physiochemical tracer characteristics on the gas-exchange rates can be studied in detail through transfer velocity measurements of individual species provided by the method proposed here. Such studies aim to improve our understanding of air–sea gas transfer and provide new insights into the theoretical background.

Gas transfer velocities have been determined in both field studies (using mass balance, eddy correlation or controlled flux techniques) and laboratory experiments described in previous gas-exchange reviews (Jähne and Haußecker, 1998; Donelan and Wanninkhof, 2002; Wanninkhof et al., 2009; Jähne, 2009; Nightingale, 2009) and references therein. Wind–wave tanks, in contrast to the open ocean, offer a unique environment for the investigation of individual mechanisms related to the air–sea gas exchange under controlled conditions.

Mass balance methods have been applied in the field using geochemical tracers (O_2, ^{14}C, Radon, for instance in Broecker et al., 1985) and dual tracer (SF_6, ^3He, for instance in Watson et al., 1991; Wanninkhof et al., 1993) techniques. The main drawback of these approaches was the relatively low temporal resolution (Jähne and Haußecker, 1998). Furthermore, the transfer velocity measurements were based primarily on sparingly soluble tracers, and very few experimental results of highly soluble trace gas transfer velocities are available.

In this study, gas-exchange experiments were performed in a state-of-the-art large-scale annular wind–wave tank. An experimental approach based on mass balance has been developed, whereby air- and water-side concentrations of various tracers are monitored using instrumentation capable of online measurement. For the first time, parallel measurements of total air and water-side transfer velocities for 14 individual gases within a wide range of solubility, have been achieved. Wind speed conditions (reported at 10 metres height, u_{10}) as low as 0.73 and reaching up to 13.2 m s^{-1} were investigated. Supplementary parameters directly linked with the gas-exchange velocities, such as friction velocity and mean square slope of the water surface, were additionally measured under the same conditions. This paper details the entire instrumental set-up and provides a validation of the overall operation and concept through transfer velocity measurements of nitrous oxide and methanol. These species are chosen as they bracket the wide range of solubilities among the investigated tracers and clearly show different gas-exchange behaviours. Transfer velocity measurements of the remaining examined tracers are going to be presented in a follow-up publication.

2 Method

In this study, total transfer velocities for low as well as medium to highly soluble tracers were determined using a mass balance approach. The wind–wave tank is interpreted in terms of a box model.

2.1 The box model

The basic idea of the box model method is the development of a direct correlation between the air- and water-phase concentrations, c_a and c_w, and the desired transfer rates, k_t, of various inert tracers.

Figure 1 shows a schematic representation of the wind–wave tank in a box model (Kräuter, 2011; Krall, 2013). Water and air spaces are assumed to be two well-mixed separate boxes with volumes, V_w and V_a, between which tracers can be exchanged only through the water surface, A. Further possible pathways of tracers entering or leaving the box are also shown in Fig. 1. Assuming constant volumes, temperature and pressure conditions, the mass balance for the air and the water phases of the box yields for a water-side perspective:

$$V_a \dot{c}_a = A k_{tw}(c_w - \alpha c_a) + \dot{V}_a^i c_a^i - \dot{V}_a c_a + \dot{V}_a c_a^0 \quad (1)$$

$$V_w \dot{c}_w = -A k_{tw}(c_w - \alpha c_a) \quad (2)$$

and an air-side perspective:

$$V_a \dot{c}_a = -A k_{ta}\left(c_a - \frac{c_w}{\alpha}\right) + \dot{V}_a^i c_a^i - \dot{V}_a c_a + \dot{V}_a c_a^0 \quad (3)$$

$$V_w \dot{c}_w = A k_{ta}\left(c_a - \frac{c_w}{\alpha}\right), \quad (4)$$

where $\alpha = c_w/c_a$ denotes the dimensionless solubility and k_{tw}, k_{ta} the total transfer velocities for a water- and an air-sided viewer, respectively. The two transfer velocities differ by the solubility factor of the tracer (see Eq. A1 in Appendix A). The dotting stands for the time derivative of the related symbol.

The first term on the right hand side of each equation represents the exchange of a tracer from one phase to the other due to a concentration gradient. The second term stands for possible tracer input ($\dot{V}_a^i c_a^i$), the third term for possible tracer output (flushing/leaking term: $\dot{V}_a c_a$) and the fourth term for a possible tracer coming in through leaks from the surrounding room or through the flushing ($\dot{V}_a c_a^0$).

In the following sections, two different box model solutions, as used in this work for the low solubility tracers (water-side controlled: Sect. 2.2) and for the medium to

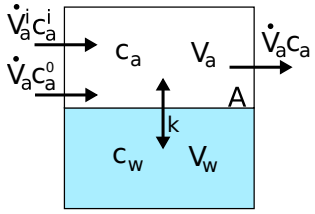

Figure 1. Mass balances for the air and water side. Naming convention is as follows: A: water surface area; V_a: air volume; V_w: water volume; k: gas transfer velocity; c_a: air-side concentration; c_w: water-side concentration; c_a^i: input tracer concentration; c_a^0: tracer concentration in the ambient air. The dotting denotes the time derivative of the related symbol.

high solubility tracers (air-side controlled: Sect. 2.3), are presented in detail. The simulated air/water concentration time series derived for a water-side (b and c in purple) and an air-side controlled (d and e in orange) tracer are presented in Fig. 2.

2.2 Water-side controlled tracers

The following approach was used for tracers with relatively low solubility ($\alpha < 100$) for which the transfer velocity, k_t, is mainly restricted due to the water-side resistance. Here, a low solubility tracer is dissolved in the water volume which is considered well mixed. High tracer concentration in the water and very low concentrations in the air ($c_a \simeq 0$) direct the flux from the water to the air (evasion).

Figure 2b shows the simulated air-phase concentration time series of an example water-side controlled tracer at three example wind speed conditions (as seen in Fig. 2a, change of wind speed is denoted with grey dashed lines). Each condition starts with a closed air-space tank configuration (closed box – no flushing; see more details in Sect. 3.2.5), where the air-side concentration, starting from circa zero, increases linearly with time, due to the water-to-air gas exchange. At time t_1, the air space is opened (open box – flushing on; flushing time is denoted with grey background) and a drastic decrease is observed due to dilution of the air-space concentration with the relatively clean ambient air entering the facility. As indicated in the figure, the higher the wind speed the faster the concentration increase. Figure 2c presents the water-phase concentration of the same tracer which in parallel starts from the highest concentration point and gradually decreases during the course of the experiment as more and more molecules escape the water to enter the gas phase.

The ambient tracer concentration in the air entering the air space through leaks or during flushing can be safely assumed as negligible in comparison to the levels used for all examined tracers. Omitting parameter c_a^0, simplifies the box model Eq. (1), which can be subsequently solved for k_{tw} as follows:

$$k_{tw} = \frac{V_a}{A} \cdot \frac{\dot{c}_a + \lambda_{f,x} c_a}{c_w} \cdot \frac{1}{1 - \alpha c_a / c_w}, \quad (5)$$

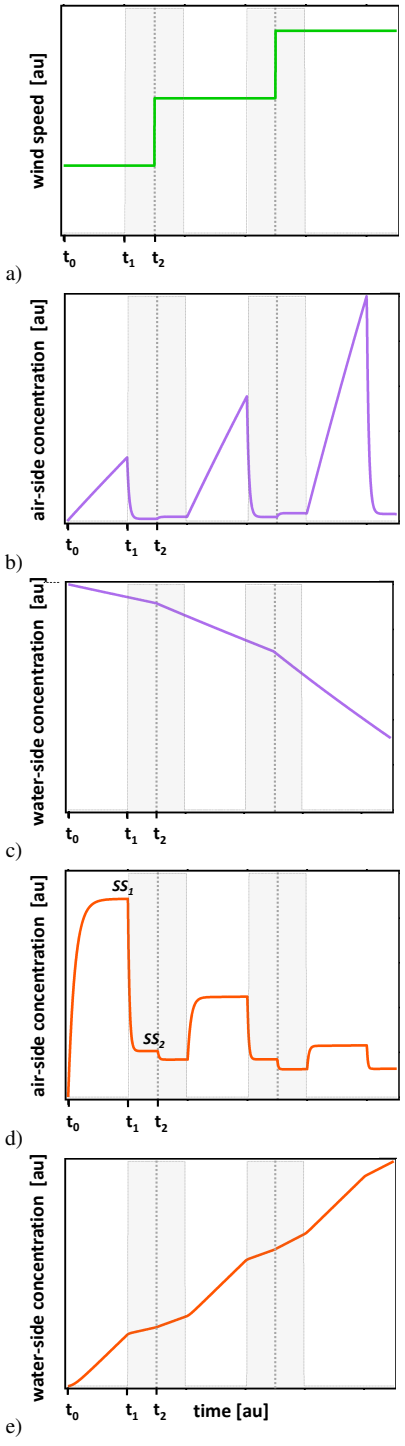

Figure 2. Simulated concentration time series for a water (**b** and **c**) and an air-side controlled (**d** and **e**) tracer in both air and water phase, at three example wind speed conditions. The grey background denotes the air-phase flashing periods and the dashed lines the change of the wind speed condition. SS_1 and SS_2 mark the developed steady states.

where $\lambda_{f,x} = \dot{V}_a/V_a$ is the leak or flush rate for x being 1 or 2, respectively.

Applying Eq. (5), the instantaneous total transfer velocities (k_{tw}) can be calculated from time-resolved measurements of air- and water-side concentrations.

2.3 Air-side controlled tracers

In this approach, tracers with relatively high solubility ($\alpha > 100$) for which k_t is expected to be controlled mainly by air-side processes, were used. Here, a relatively high solubility tracer is introduced with a constant flow to the air volume, continuously during the experiment. Due to low concentrations in the water volume, the net gas-exchange flux is directed from the air to the water (invasion).

In Fig. 2d the air-phase concentration of an example air-side controlled tracer is shown. During the closed air-space period (t_0 to t_1), the concentration increases exponentially, as a fraction of the air-space molecules transmit into the water due to the air–water gas exchange. At t_1, the concentration reaches a steady state, SS_1, where the input rate of the tracer is equal to the exchange rate between the two phases and the leak/flush rate.

At an equilibrium point, the concentration time derivative $\dot{c}_a$ is approximately zero so that Eq. (3) can be written as

$$c_a = \frac{\lambda_{ta}\frac{c_w}{\alpha} + \lambda^i c_a^i}{\lambda_{ta} + \lambda_{f,x}}, \quad (6)$$

where $\lambda_{ta} = \frac{A}{V_a}k_{ta}$ is the exchange rate and $\lambda^i = \frac{\dot{V}_a^i}{V_a}$ the input rate.

After SS_1, the facility is flushed with ambient air (open air space) and the concentration decreases abruptly. Under these conditions (t_2), a second steady state, SS_2, is developed at a lower concentration range. In SS_1, a very small leak rate is present ($\lambda_{f,1} \approx 0$, leak rate) while in SS_2 the leak rate is much larger due to the open air space ($\lambda_{f,2}$, flush rate). Dividing the air-side concentrations of the two steady states $\frac{c_{a,1}}{c_{a,2}}$ (as given in Eq. 6) and solving it with respect to the exchange rate yields

$$\lambda_{ta} = \frac{\lambda_{f,2}c_{a,2} - \lambda_{f,1}c_{a,1}}{(c_{a,1} - c_{a,2})}. \quad (7)$$

The total transfer velocities in the wind–wave tank box are calculated from

$$k_{ta} = \frac{\lambda_{ta}V_a}{A}. \quad (8)$$

2.3.1 Leak and flush rate

In most wind–wave facilities, small air leaks are inevitable. The amount of tracer escaping the air space of the facility needs to be monitored and corrected for, as described in Sects. 2.2 and 2.3. To measure the leak/flush rate $\lambda_{f,x}$ for the open and closed configuration of the wind–wave tank, a non-soluble tracer (here CF_4), called a leak test gas, is used. Directly after closing the wind–wave tank, a small amount of the leak test gas is injected rapidly into the air space. As the leak test gas is non-soluble, the water-side concentration, c_w, as well as the gas-exchange velocity, k_{ta}, in Eq. (3) are equal to zero, reducing the air-side mass balance equation to

$$V_a\dot{c}_a = \dot{V}_a^i c_a^i - \dot{V}_a c_a. \quad (9)$$

After the initial injection, the input term $\dot{V}_a^i c_a^i$ in Eq. (9) vanishes, yielding $V_a\dot{c}_a = -\dot{V}_a c_a$. This simple differential equation can be solved easily with

$$c_a(t) = c_a(0) \cdot \exp(-\lambda_{f,x} \cdot t), \quad (10)$$

where $c_a(0)$ is the concentration directly after the input of the leak test gas. Monitoring the concentration of the leak test gas over time and fitting an exponentially decreasing curve to this concentration time series yields the leak/flush rate $\lambda_{f,x}$ of the system. In the Aeolotron facility, typical leak and flush rates were of the order of 0.05 to 0.4 h^{-1} and 20 to 50 h^{-1}, respectively.

3 Experiments

3.1 The Aeolotron wind–wave tank

The air–water gas-exchange experiments were conducted in the large-scale annular Aeolotron wind–wave tank at the University of Heidelberg, Germany (Fig. 3). With an outer diameter of 10 m, a total height of 2.4 m and a typical water volume of 18 000 L, the Aeolotron represents the world's largest operational ring shaped facility (much larger than annular facilities used in previous investigations, Jähne et al., 1979, 1987). The chamber is mostly gastight, thermally isolated, chemically clean and inert. In Fig. 3, a list of the main dimensions along with an aerial illustration of the facility are given. The tank is divided in 16 segments and an inner window extending through segments 16 to 4 allows visual access to the wind formed waves. The facility ventilation system consists of two pipes through which the air space can be flushed with ambient air at a rate of up to 50 h^{-1}. Two diametrically positioned ceiling mounted axial ventilators (segment 4 and 12) are used to generate wind velocities of up to $u_{ref} = 12\,m\,s^{-1}$.

In the facility, several ambient parameters are monitored. Temperature measurements are provided by two temperature sensors (PT-100) installed in the water and air phase of segment 15 (at heights of 0.5 and 2.3 m, respectively). On the ceiling of the same segment a fan anemometer (STS 020 by Greisinger electronic GmbH) installed in the centre line, determines the wind velocity. Two humidity sensors are mounted in segments 2 and 13. An optical ruler provides the water height using the principle of communicating vessels. Segments 1 and 11 contain the tracer inlets for the air and water phase, respectively. The leak test gas is introduced in segment 11.

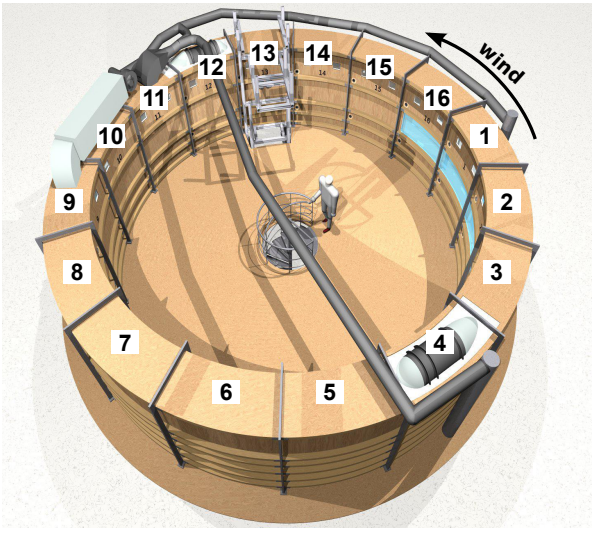

Main Features	
mean circumference	29.2 m
mean diameter	9.3 m
mean width	61 cm
mean total height	241 cm
typical water depth	100 cm
surface area	17.9 m^2
typical water volume	17.9 m^3
typical air volume	24.4 m^3

Figure 3. An aerial illustration of the Aeolotron tank and its main features. The numbers denote the segments. The axial fans producing the wind can be seen in the roof of segments 4 and 12. The air pipes supplying fresh air and removing waste air are shown in grey; figure adapted from (Krall, 2013)).

The annular geometry of the wind–wave tank, contrary to a linear geometry, permits homogeneous wave fields and unlimited fetch. The well-mixed air space (at few centimetres height above the surface) ensures no concentration gradients and therefore concentration measurements independent of the sampling height. On the other hand, the restricted size of the facility which leads to waves reflecting off the walls, results with a different wave field to that found in the open ocean.

3.2 Tracers and instrumentation

A series of 14 tracers covering a wide solubility ($\alpha = 0.4$ to 5470) and diffusivity ($Sc_w = 594$ to 1194) range, were selected for this study. Many of these tracers are very common in the ocean environment, while the rest are used to extend the solubility and diffusivity ranges, a significant criterion for further physical investigations of the gas-exchange mechanisms. Table 1 gives an overview of the examined tracers, with their respective molecular masses, solubility and Schmidt numbers, Sc (the dimensionless ratio of the kinematic viscosity of water ν and the diffusivity of the tracer D, $Sc = \nu/D$) at 20 °C.

All tracers were monitored on-line in both the air and the water phase. The VOC measurements were performed using proton reaction mass spectrometry (PTR-MS) from Ionicon Analytik GmbH (Innsbruck, Austria), while for the halocarbons and N_2O, two Fourier transform infrared (FT-IR) Spectrometers (Thermo Nicolet iS10) were used. As leak test gas, carbon tetrafluoride (CF_4) was used; it was also measured by FT-IR spectrometry.

For the surfactant experiments, the soluble substance Triton X-100, $C_{14}H_{22}O(C_2H_4O)_{9.5}$ (Dow Chemicals, listed $M_r = 647\,g\,mol^{-1}$) was used to cover the water surface. Triton X-100 was chosen because of its common use as a reference substance to quantify the surface activity of unknown surfactant mixtures found in the open ocean (Frew et al., 1995; Cosovic and Vojvodic, 1998; Wurl et al., 2011).

The operation and sampling conditions for both air and water phases are briefly described below. Additional instrumentation for substantial supplementary measurements follows.

3.2.1 Water-phase measurements

In the water phase a PTR-Quadrupole-MS (PTRQ-MS) (water inlet in segment 3) and a FT-IR spectrometer (water inlet in segment 6) were used to measure the concentration levels of the VOCs and the halocarbons and N_2O, respectively. Our instrumentation, which is normally suited only for air sampling, was combined with an external membrane equilibrator (the oxygenator Quadrox manufactured by Maquet GmbH, Rastatt, Germany) to establish equilibrium between the water concentration and the gas stream to be measured. In this way, water-side concentrations could be obtained and used for the calculation of the transfer velocities for the low solubility tracers (see Sect. 2.2).

Membrane equilibrator configuration

The membrane equilibrator device includes a thin gas permeable membrane capable of separating the gas from the liquid phase (commercially available and often used in medicine as a human lung replacement to oxygenate blood). Water from the Aeolotron is constantly pumped through the membrane device. Inside the equilibrator gas exchange occurs, due to

Table 1. Molecular masses (M in g mol^{-1}), dimensionless solubility (α) and Schmidt numbers in air (Sc_a) and water (Sc_w) for the investigated tracers at 20 °C.

Gas	Formula	M	α	Sc_a^l	Sc_w^l
methanol	CH_3OH	32.04	5293[a]	1.0268	671.04
1-butanol	C_4H_9OH	74.12	4712[b]	1.8198	1141.7
acetonitrile	CH_3CN	41.05	1609[c]	1.2957	832.07
acetone	$(CH_3)_2CO$	58.08	878.0[c]	1.4921	880.53
2-butanone	$C_2H_5COCH_3$	72.11	598.9[b]	1.7344	1159.8
acetaldehyde	CH_3CHO	44.05	378.7[d]	1.0786	824.90
ethyl acetate	$CH_3C(O)OC_2H_5$	88.10	156.4[e]	1.8183	997.46
dms	CH_3SCH_3	62.13	16.62[f]	1.4484	979.40
benzene	C_6H_6	78.11	5.672[g]	1.6785	980.46
toluene	$C_6H_5CH_3$	92.14	4.529[g]	1.8409	1176.3
trifluoromethane	CHF_3	70.01	0.760[h]	1.2132	747.50
nitrous oxide	N_2O	44.01	0.676[i]	1.0007	593.90
isoprene	C_5H_8	68.12	0.31[j]–0.69[k,*]	1.6617	1193.9
pentafluoroethane	CF_3CHF_2	120.0	0.415[h]	1.5106	1027.0

[a] Schaffer and Daubert (1969), [b] Snider and Dawson (1985), [c] Benkelberg et al. (1995), [d] Betterton and Hoffmann (1988), [e] Janini and Quaddora (1986), [f] Dacey et al. (1984), [g] Robbins et al. (1993), [h] Krall (2013), [i] Weiss and Price (1980), [j] Yaws and Pan (1992), [k] Sander (1999), [l] Yaws (1995), * only available values at 25 °C.

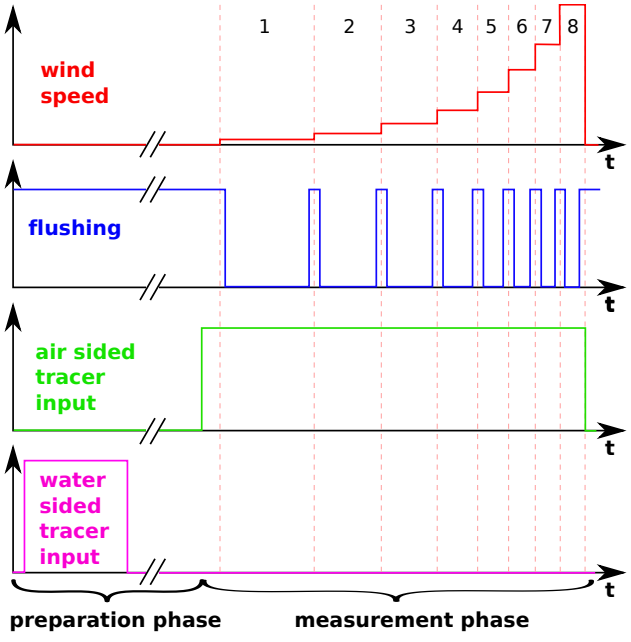

Figure 4. Schematic time series of the wind speed, flushing periods and air/water tracer inputs.

the partial pressure difference of the gases involved, until equilibrium between air and water is achieved (Henry's law at constant temperature).

A detailed configuration of the membrane set-up in conjunction with the PTR-MS is shown in Fig. 6. The system consists of a water and an air loop, both constantly in contact with the membrane equilibrator. The dark blue lines represent the water loop where water was being pumped from the Aeolotron through the membrane and back into the facility, with a constant flow of 3.4 L min^{-1}. The light orange coloured lines represent the air loop which has a link to the PTRQ-MS instrument. A synthetic air inlet and an excess flow exhaust are used to regulate the flow inside the air loop constant at 1 L min^{-1} and the systems pressure at 1013 hPa. Part of the air that comes out of the equilibrator is driven to the PTRQ-MS for analysis, while the rest remains in the loop. The relative humidity in the equilibrated air increases after passing through the equilibrator; therefore, the air tubing was heated to a few degrees above room temperature to avoid water condensation.

A similar set-up using a second membrane equilibrator was connected to the FT-IR instrument. The water flow was kept at a rate of about 3 L min^{-1}. Here the instrument's measuring cell was integrated into the air loop, removing the need for sample extraction, a synthetic air inlet and an exhaust. The air was circulated in the closed loop at a rate of approximately 150 mL min^{-1}. Between the equilibrator and the measuring cell, a dehumidifying unit containing phosphorous pentoxide was used to remove water from the air stream and in this way protect the optical windows of the IR measuring cell.

The time constant of the membrane equilibrator was evaluated as described in Krall and Jähne (2014), providing a very fast response of $\simeq 1$ min.

PTRQ-MS configuration

The PTR-MS detection technique has been described in detail elsewhere (Lindinger et al., 1998). Here, a PTRQ-MS

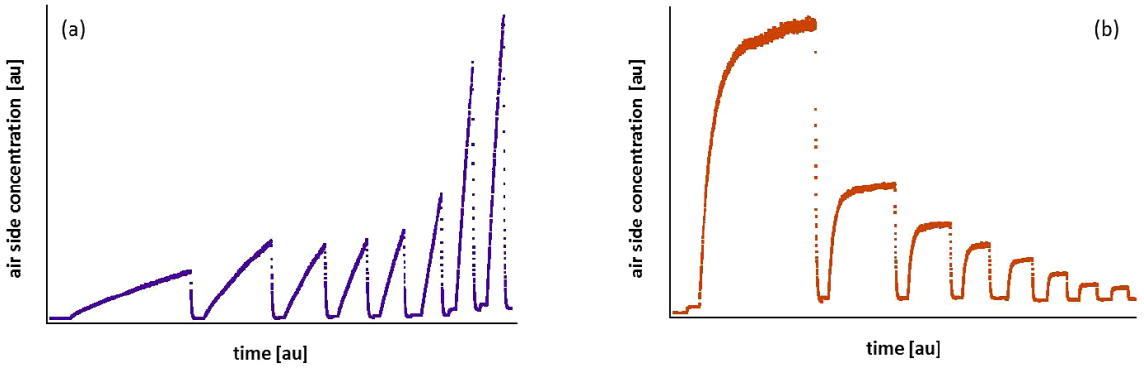

Figure 5. Air-side concentrations obtained for example water-side **(a)** and air-side **(b)** controlled tracers throughout the experimental procedure.

was operated under 30 mL min^{-1} sampling flow, 2.1 mbar drift pressure, and 600 V drift voltage (E / N = 130 Td, Td = 10^{-17} cm^2 V molecule^{-1}). A total of 30 masses were measured sequentially with a dwell time of 1 s (time resolution is 30 s). Possible mass overlapping was prevented by the careful reselection of the analysed compounds based on the initial mass scan.

Water-phase calibrations were performed in conjunction with the membrane equilibrator set-up (see Fig. 6). Known VOC concentrations were diluted in deionised water and then introduced into the water phase of the facility, in precise volume quantities. To avoid losses of the investigated tracers into the air phase due to air–water gas exchange, the water surface was covered with a large amount of an organic surfactant (0.446 mg L^{-1}, Triton X-100) and calm wind conditions were used to gently mix the air space. Under such conditions gas-exchange velocities were estimated to be negligible. Linear behaviour was established for all examined tracers at concentration levels embracing the characteristic water-phase concentration ranges detected during the experiments.

FT-IR configuration

The key aspects of FT-IR spectroscopy are described in detail in Griffiths (2007). In this study, a Nicolet iS10 (manufactured by Thermo Fischer Scientific Inc., Waltham, MA., USA) FT-IR spectrometer with a custom made measuring cell of approximately 5 cm length was used. About every 5 s, one infrared absorbance spectrum with wave numbers between 4000 and 650 cm^{-1} with a resolution of 0.214 cm^{-1} was acquired. Six of these single spectra were averaged to minimise noise and stored for further evaluation, leading to a time resolution of about 1 spectrum every 30 s. Signal conversion to water-phase concentration, calibration and uncertainty estimation are described in detail in Krall (2013).

3.2.2 Air-phase measurements

In the air phase, a PTR-time of flight (ToF)-MS (inlet in segment 3) with a time resolution of 10 s provided very fast on-line measurements for the VOCs while a FT-IR (inlet in segment 2) with a time resolution of 30 s was in parallel monitoring the halocarbons and N_2O. High time resolution measurements enabled a fast experimental procedure and at the same time high accuracy data analysis. Additionally, due to the fast on-line measurements, the transient response of the system could be followed very efficiently throughout the experimental procedure. Example air-side measurements are shown in Fig. 5 for a water and an air-side controlled tracer.

PTR-ToF-MS configuration

The ionisation principle of the PTR-ToF-MS is the same as the PTRQ-MS; however, here a time-of-flight mass spectrometer is used. Throughout the measurements, the PTR-ToF-MS was configured in the standard V mode with a mass resolution of approximately 3700 m Δm^{-1}. The drift voltage was maintained at 600 V and the drift pressure at 2.20 mbar (E / N 140 Td). Mass spectra were collected over the range 10–200 m/z (mass-to-charge ratio) and averaged every 10 s, providing a mean internal signal for each compound. After acquisition all spectrum files were mass calibrated using $(H_2O)H^+$, NO^+ and $(C_3H_6O)H^+$ ions to correct for mass peak shifting.

Calibrations in the air phase were conducted under high humidity conditions equivalent to the sampling conditions during the experiments (85–90 % RH). The desired mixing ratios (1–600 ppbv) were obtained by appropriate dilution of the multi-component VOC gas standard with synthetic air. Linear response was established for all examined tracers.

FT-IR configuration

A second Thermo Scientific Nicolet iS10 FT-IR spectrometer was used to measure the air-side concentrations. The measuring cell with a folded light path of a total length of 2 m,

was kept at a constant temperature of 35 °C using a Thermo Nicolet cell cover. Air from the Aeolotron was sampled at a rate of 150 min^{-1} at segment 13. As with the water-side instrumentation, water vapour was removed before entering the measuring cell using phosphorous pentoxide. The spectrometer settings, data acquisition as well as data processing, were identical to the water-side instrumentation, see Sect. 3.2.1.

3.2.3 Error analysis of k_t

The individual total transfer velocity uncertainties were calculated applying the propagation of error for uncertainties independent from each other to Eq. (5) for the k_{tw}, and Eqs. (7) and (8) for the k_{ta}.

The concentration uncertainties for the PTR-MS measurements were calculated using the background noise and the calibration uncertainty of each examined tracer. Relatively low uncertainties were obtained for the air-phase concentration levels SS_1 and SS_2 ranging between 1–1.5 % and 1.5–2.5 %, respectively. The water-phase concentration uncertainty, Δc_w, was estimated the same way and the uncertainties were between 6.5 and 8 % for the concentration ranges used.

The uncertainty of the concentration measurement with the FT-IR spectrometers was found to be concentration dependent. All concentration uncertainties lie below 4 % for the typical concentrations measured in the described experiments.

The individual uncertainties for the leak and flush rates of all conditions were of the order of 0.5 and 1 %, respectively. Based on the geometrical parameters of the facility the surface area uncertainty was calculated to be approximately 2 %, while a maximum of 3 % is estimated for the volume uncertainty. For the solubility values provided by literature, accurate uncertainty estimations are difficult. Here we assume a maximum uncertainty of 10 % for all literature sources.

The overall estimated total transfer velocity uncertainties therefore ranged between 6–12 and 6–20 %, respectively, for the k_{ta} and k_{tw} values of all examined tracers.

3.2.4 Additional instrumentation

Supplementary measurements of wind driven, surface associated, physical parameters, such as the mean square slope and the water-sided friction velocity, were additionally made in the Aeolotron wind–wave tank to enable further investigations of the physical mechanisms of air–water gas exchange.

The mean square slope measurements, reflecting the surface roughness conditions, were performed in parallel with the gas-exchange measurements using a colour imaging slope gauge (CISG) installed in segment 13. The CISG device uses the refraction properties of light at the air–water boundary. A colour coded light source was placed below the water while a camera observed the water surface from above. Using lenses to achieve a telecentric set-up, a relationship between surface slope and the registered colour can be determined. Errors are calculated from the statistical fluctuations of the individually measured mean square slope values. A more detailed description can be found in Rocholz (2008).

The water-sided friction velocity, $u_{*,w}$, measurements, expressing the shear stress created on the water interface, were accomplished at a later stage using the same setting of the wind generator and the same surfactant coverage of the water surface. The momentum balance method was used as described in Bopp (2014) and Nielsen (2004). To apply this method, the friction between the water and the walls needs to be measured first. This is done by monitoring the decrease of the velocity of the bulk water after switching off the wind. In a stationary equilibrium, that is characterised by an equality of the momentum input into the water by the wind and the momentum loss due to friction at the walls, the friction velocity, $u_{*,w}$, can be calculated from the mean water velocity. The water velocity was measured using a three-axis Modular Acoustic Velocity Sensor (MAVS-3 manufactured by NOBSKA, Falmouth, MA, USA) installed in the centre of the water channel in segment 4 of the Aeolotron at a water depth of around 50 cm. The uncertainty of the friction velocity measurements is calculated from the statistical fluctuations of the bulk water velocity measurement as well as the uncertainty in the friction parameter used in the momentum balance method. Both sources of error are described in detail in Bopp (2014). Subsequently, simple error propagation was used to derive the wind speed (u_{10}) uncertainty from the Smith and Banke (1975) empirical relationship (see Appendix B), the error of which is assumed to be negligible.

3.2.5 Experimental arrangement

The Aeolotron facility was filled to 1 m height ($\sim 18\,\mathrm{m}^3$ water volume) with clean deionised water. Diluted aqueous mixtures of low solubility tracers were introduced into the water phase of the facility a day prior to an experiment and homogeneity was achieved using two circulating pumps. Before the beginning of each experiment (for the clean water surface cases), the water surface was skimmed to clean off any possible surface contamination. To do this, a small barrier with a channel is mounted between the walls of the tank, perpendicular to the wind direction while the wind is turned on at a low wind speed ($u_{ref} \approx 3\,\mathrm{m\,s}^{-1}$). The wind pushes the water surface over the barrier into the channel removing any surfactant. A pump continuously empties the channel and drains the water contaminated with surface active materials.

Individual gas-washing bottles containing highly solubility tracers in liquid form were purged with a controlled flow of clean air that swept the air-tracer gas mixture into the air phase of the facility. The bottles were kept in a thermostatic bath at 20 °C throughout the experimental procedure.

At the beginning of each experiment, the first wind speed condition was applied while the flushing of the air space was turned on (open air space) in order to achieve a background

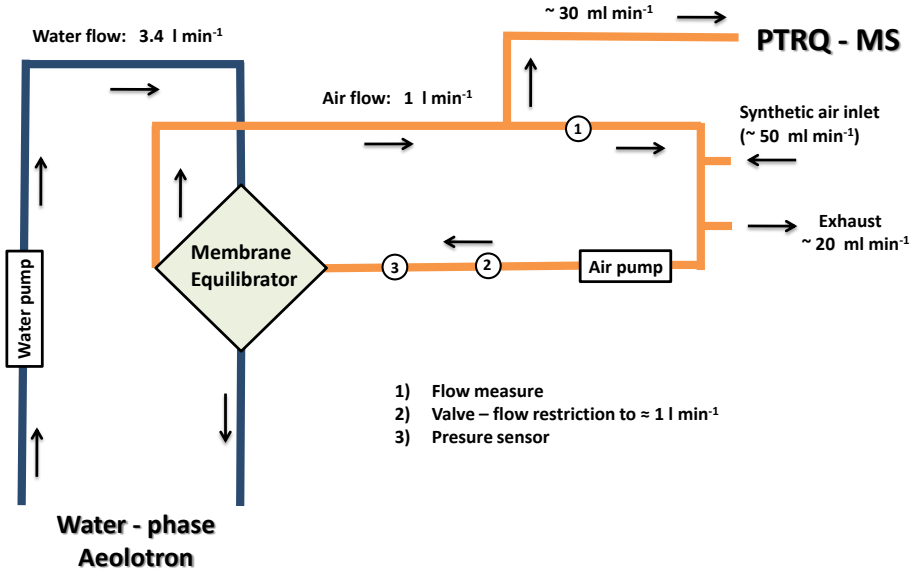

Figure 6. Membrane equilibrator – PTRQ-MS set-up schematic. The dark blue and orange lines represent the water and air loops of the system, accordingly.

point for all tracers. Thereafter, the flushing was turned off (closed air space) and the tracer concentration (air and water-side controlled) started to increase (see more in Sect. 2.3). Immediately after turning off the flushing, the leak test gas was introduced into the air space. After the steady-state point (SS_1) for the air-side controlled tracers was approached, the air space was flushed once more with ambient air and an abrupt concentration decrease was observed. The same process was repeated for eight different wind speed conditions, progressing from lower to higher values. In Fig. 4 a time series of the experimental conditions (wind speed, flushing periods and air and water tracer inputs) are schematically represented. The obtained air-sided concentration time series over the eight wind speed conditions for a water- and an air-sided example tracer are given in Fig. 5.

The wind speed varied from very low values ($u_{\mathrm{ref}} = 0.74\,\mathrm{m\,s^{-1}}$, equivalent to $u_{10} = 0.73\,\mathrm{m\,s^{-1}}$) up to higher ones ($u_{\mathrm{ref}} = 8.26\,\mathrm{m\,s^{-1}}$, equiv. $u_{10} = 13.2\,\mathrm{m\,s^{-1}}$). At the very beginning of the experiment, hardly any surface movement was seen. As the experiment progressed, the first capillary waves became apparent and started breaking above $u_{\mathrm{ref}} = 4.8\,\mathrm{m\,s^{-1}}$, equiv. $u_{10} = 6.6\,\mathrm{m\,s^{-1}}$. Reaching larger wavelengths, wave braking and bubble formation was observable only at the highest wind speed condition.

The experimental procedure described above was repeated four times at clean surface conditions for all tracers listed in Table 1. Three further repetitions were accomplished with a surfactant (Triton X-100) covered water surface. The surfactant concentration in the fifth repetition was $0.033\,\mathrm{mg\,L^{-1}}$ while in the last two a larger amount of $0.167\,\mathrm{mg\,L^{-1}}$ was used.

Despite the well-reproduced experimental conditions, small variations between the repetitions were observed. Table 2 displays a mean value of the main measured parameters along with the standard deviation, expressing the extent of variability between the repetitions, of each case. For the highest wind speed condition of the clean case, only three repetitions were performed. Also in repetition two, the σ_s^2 values observed in conditions 4, 5 and 6 were significantly lower and therefore omitted from the averaging. Here we assume that the water surface was probably insufficiently skimmed before the experiment or that surfactant material might have entered the facility during the flushing phases. In the higher surfactant case (case 3), the first condition was omitted for reasons of experimental simplicity while σ_s^2 are available only for one repetition.

4 Results

In this work, total transfer velocities of two contrasting tracers at opposite ends of the solubility spectrum, N_2O ($\alpha = 0.67$) anticipated as only water-side controlled (i.e $k_{\mathrm{tw}} \sim k_{\mathrm{w}}$) and CH_3OH ($\alpha = 5293$) similarly anticipated as only air-side controlled (i.e. $k_{\mathrm{ta}} \sim k_{\mathrm{a}}$), are presented. In this way, we intend to validate the above described method and apparatus and subsequently to compare with previous air–sea gas-exchange studies. A full investigation of the mechanisms influencing the gas-exchange transfer and their relationship to individual gases over a broad solubility range will be presented in separate publications.

Table 2. Reference velocities, u_{ref} ($\mathrm{m\,s^{-1}}$), friction velocities, $u_{*,\mathrm{w}}$ ($\mathrm{cm\,s^{-1}}$), mean square slope, σ_{s}^2, air temperature, t_{a} (°C), water temperature, t_{w} (°C) mean values and % standard deviations as quantified in the Aeolotron facility for case 1: clean surface experiments; case 2: surface covered with $0.033\,\mathrm{mg\,L^{-1}}$ Triton X-100; and case 3: surface covered with $0.167\,\mathrm{mg\,L^{-1}}$ Triton X-100, at eight different wind speed conditions. The number of replicates used for each case is given in brackets.

Case	Parameter	Cond.1	Cond.2	Cond.3	Cond.4	Cond.5	Cond.6	Cond.7	Cond.8
	u_{ref} (±%)	0.744 (1.3)	1.421 (0.5)	2.052 (0.3)	2.674 (0.5)	3.621 (0.1)	4.805 (0.3)	6.465 (0.2)	8.256 (0.1)
	$u_{*,\mathrm{w}}$ (±%)	0.063 (1.4)	0.135 (0.6)	0.216 (0.4)	0.309 (0.6)	0.473 (0.2)	0.720 (0.5)	1.141 (0.3)	1.967 (0.1)
1	σ_{s}^2 (±%)	0.002 (1.7)	0.007 (1.4)	0.013 (1.2)	0.016 (0.5)	0.024 (2.2)	0.046 (2.0)	0.078 (3.0)	0.118 (6.3)
(× 4)	t_{a} (±%)	21.29 (1.5)	21.18 (1.5)	21.09 (1.6)	20.99 (1.6)	20.88 (1.6)	20.75 (1.6)	20.59 (1.7)	20.50 (1.8)
	t_{w} (±%)	19.30 (1.7)	19.37 (1.8)	19.41 (1.8)	19.41 (1.8)	19.39 (1.8)	19.34 (1.9)	19.29 (2.0)	19.26 (2.1)
	u_{ref} (±%)	0.800 (–)	1.460 (–)	2.091 (–)	2.717 (–)	3.650 (–)	4.851 (–)	6.502 (–)	8.288 (–)
	$u_{*,\mathrm{w}}$(±%)	–	0.163 (–)	0.246 (–)	0.336 (–)	0.484 (–)	0.698 (–)	1.038 (–)	1.464 (–)
2	σ_{s}^2 (±%)	0.002 (–)	0.002 (–)	0.002 (–)	0.008 (–)	0.010 (–)	0.020 (–)	0.071 (–)	0.111 (–)
(× 1)	t_{a} (±%)	22.11 (–)	22.04 (–)	21.94 (–)	21.77 (–)	21.64 (–)	21.44 (–)	21.19 (–)	21.11 (–)
	t_{w} (±%)	19.80 (–)	19.88 (–)	19.93 (–)	19.93 (–)	19.93 (–)	19.90 (–)	19.88 (–)	19.85 (–)
	u_{ref} (±%)	–	1.451 (1.2)	2.075 (0.0)	2.707 (0.6)	3.667 (0.3)	4.913 (0.4)	6.615 (0.2)	8.371 (0.0)
	$u_{*,\mathrm{w}}$ (±%)	–	0.18 (1.0)	0.239 (0.0)	0.295 (0.5)	0.381 (0.3)	0.524 (0.7)	0.84 (0.4)	1.407 (0.1)
3	σ_{s}^2 (±%)	–	0.002 (–)	0.002 (–)	0.002 (–)	0.005 (–)	0.007 (–)	0.040 (–)	0.096 (–)
(× 2)	t_{a} (±%)	–	21.51 (1.4)	21.59 (1.3)	21.60 (1.0)	21.53 (0.9)	21.51 (0.6)	21.34 (0.7)	21.22 (0.9)
	t_{w} (±%)	–	19.83 (0.5)	19.86 (0.6)	19.90 (0.7)	19.94 (0.6)	19.95 (0.7)	19.95 (0.7)	19.95 (0.7)

4.1 Gas-exchange transfer velocities

In Figs. 7 and 8, we present the experimentally obtained k_{tw} for N_2O and k_{ta} for CH_3OH as a function of $u_{*,\mathrm{w}}$ for the clean water surface experiments. In both figures, the experimental results of all repetitions are nicely reproduced. Occasionally, the variation between the transfer velocity values exceeded the given uncertainty bars. A more apparent example is provided by the lower transfer velocity points (circles) at conditions 4, 5 and 6 which arise as a result of the lower σ_{s}^2 values observed in repetition 2 (as described in Sect. 3.2.5). This effect could be taken as an indication that only one physical parameter is not enough to effectively describe the complicated process of the air–sea gas exchange. As the experimental conditions used in the four repetitions were similar but not identical (see Table 2), a four replicate mean value calculation was avoided and instead a fit through all points is chosen (black dashed line).

As indicated in Fig. 7, the k_{tw} increases non-linearly with $u_{*,\mathrm{w}}$. The correlation could be described as linear up to $u_{*,\mathrm{w}} = 0.72\,\mathrm{cm\,s^{-1}}$ (equiv. $u_{10} = 6.6\,\mathrm{m\,s^{-1}}$) while above this point, a faster increase is observed. This sudden increase in the so far linear tendency can be attributed to various water surface effects (e.g. initiation of capillary wave braking), which are not going to be discussed here.

The air-sided transfer velocities k_{ta} (Fig. 8) in contrast, increase linearly ($R^2 = 0.99$) with $u_{*,\mathrm{w}}$ throughout the examined velocity range ($u_{*,\mathrm{w}} = 0.063$–$1.7\,\mathrm{cm\,s^{-1}}$ equiv. $u_{10} = 0.73$–$13.2\,\mathrm{m\,s^{-1}}$). As it appears from Fig. 8, the first transfer velocity values of CH_3OH (i.e. those at the lowest turbulent condition) are slightly underestimated relative to the linear trend ($\simeq 10\,\%$). This could be explained as being due to the inefficiently mixed air space caused by the lower turbulence conditions applied.

Overall, the observed trends and transfer velocity magnitudes of both k_{tw} and k_{ta} are in good agreement with observations made by previous studies. A more detailed comparison with literature follows in Sect. 4.3.

4.2 Effect of surfactants

After obtaining clear, reproducible transfer velocity trends for a clean water surface, the effect of a surfactant was evaluated using two different surfactant (Triton X-100) concentrations. As expected, the surfactant suppressed the transfer velocity as well as the friction velocity, $u_{*,\mathrm{w}}$, and mean square slope, σ_{s}^2 (see Table 2). In Fig. 9, the transfer velocities of all seven experiments for N_2O and CH_3OH are presented against the reference wind speed, u_{ref}; a parameter which is not affect by the surfactant layers.

As indicated in Fig. 9, the surfactant effect shows significant differences between the two contrasting tracers. A generally stronger suppression is observed for N_2O and a significantly weaker for CH_3OH where the transfer is mainly controlled by the air-side boundary layer. Under low turbulence conditions, the surfactant diminished the transfer velocity of N_2O by a factor of 3 for both examined concentrations (0.033 and $0.167\,\mathrm{mg\,L^{-1}}$ Triton X-100) (Fig. 9a). In the case of CH_3OH, the effect was weaker demonstrated by a factor of 1.5 (Fig. 9b). At slightly higher wind speeds (i.e $\geq u_{\mathrm{ref}}\,3\,\mathrm{m\,s^{-1}}$; see Table 2 for the equivalent $u_{*,\mathrm{w}}$ of each case), different trends are observed between low and high

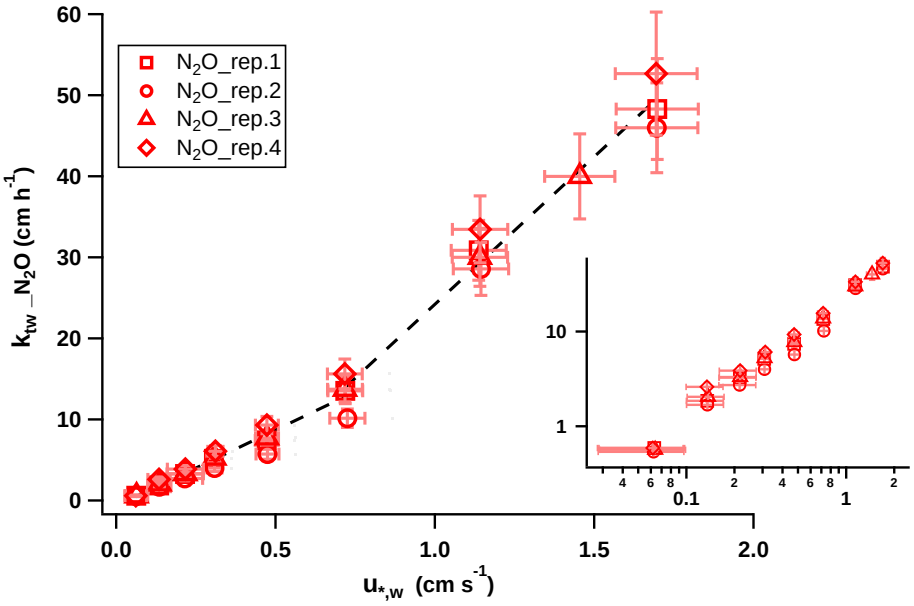

Figure 7. Total transfer velocity of N_2O of four clean case repetitions plotted against $u_{*,w}$. Squares correspond to repetition 1, circles to repetition 2, triangles to repetition 3 and diamonds to repetition 4. Vertical bars in light red give the individual transfer velocity uncertainty (see Sect. 3.2.3) and the horizontal bars the uncertainty of the $u_{*,w}$ measurements.

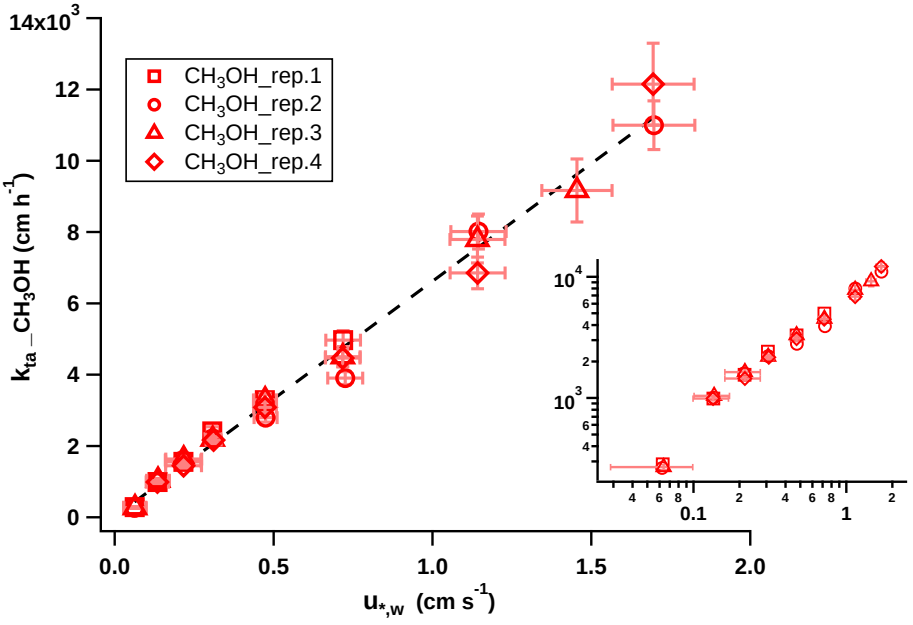

Figure 8. Total transfer velocity of CH_3OH of four clean case repetitions plotted against $u_{*,w}$. Symbols and bars are the same as in Fig. 7.

surfactant concentrations with the higher concentration causing a more prominent suppression. Reaching the highest examined wind speed where waves, wave breaking and bubbles are present, the surfactant effect is significantly weaker. In the case of CH_3OH, no further impact is observed (values within the error bars), while a still significant suppression (around a factor of 1.5) is apparent for the k_{tw} of N_2O under a 0.167 mg L^{-1} Triton X-100 surfactant film.

Reduced surface stress and roughness change the hydrodynamic properties of the water surface and consequently affect the gas transfer. As given in Table 2, the suppression caused by a surfactant seems to be relatively strong for σ_s^2 (like in the case of N_2O) and rather weak for $u_{*,w}$ (here, note the higher uncertainties at the low wind speed regime). The trend of the reduction for both $u_{*,w}$ and σ_s^2 was similar to the one of k_t, more apparent at low wind speeds and weaker under higher

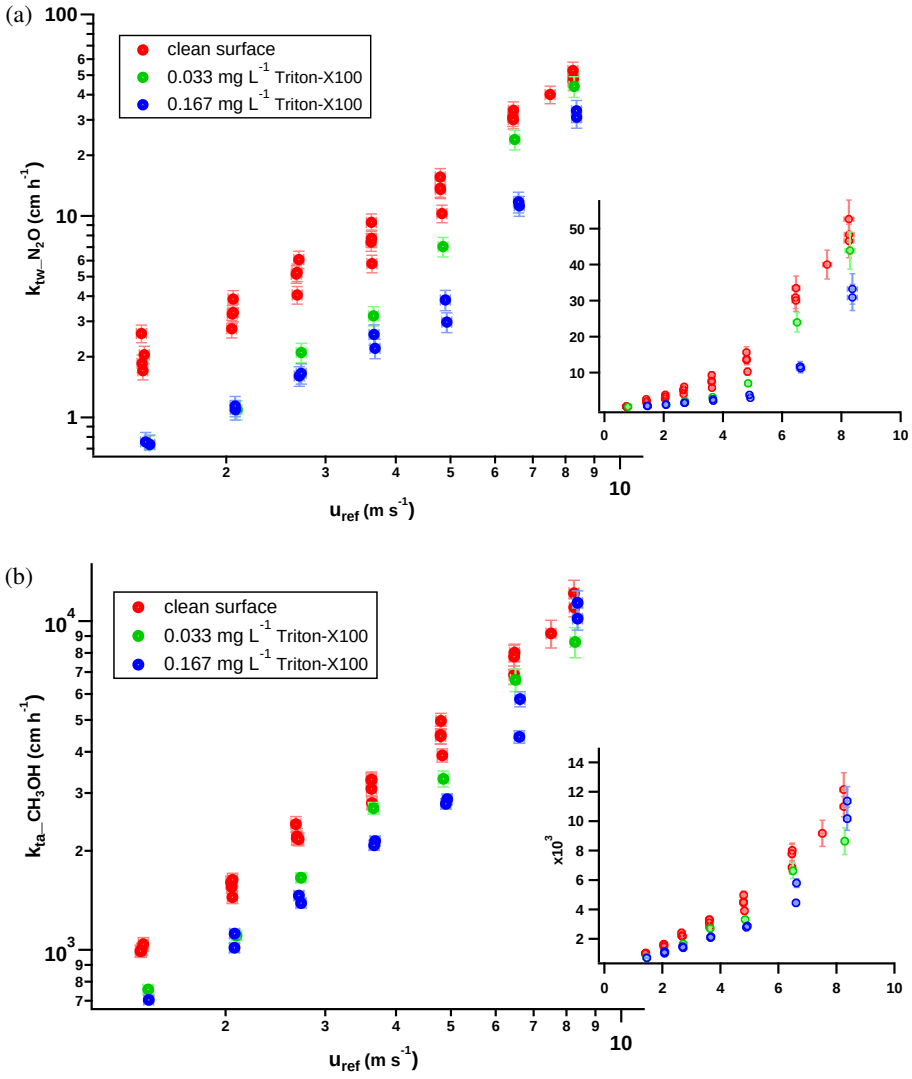

Figure 9. Effect of the two different surfactant concentrations on the total transfer velocities of **(a)** N_2O and **(b)** CH_3OH. The clean water surface results are given in red, the results obtained using 0.033 mg L^{-1} Triton X-100 in green and the ones using 0.167 mg L^{-1} Triton X-100 in blue.

turbulence. The way in which each of these parameters affect the gas transfer needs further investigation and is going to be presented in a following publication.

4.3 Comparison with previous studies

The gas transfer velocities of weakly soluble tracers has been extensively studied over the previous years. Numerous k_w parameterisations are available, derived from experimental (laboratory and field) measurements as well as physical models. In Fig. 10, a selection of some representative, experimentally derived parameterisations (coloured lines), are used for comparison with the k_{tw} (here $k_{tw} \sim k_w$) measurements of N_2O (red points). The transfer velocities are plotted against the wind speed at 10 m height, u_{10}.

Looking at the lower wind speed range (0.7 to 4 m s^{-1}) an obvious spread between the various k_w predictions can be observed extending through more than 2 orders of magnitude. Transfer velocity measurements at the very low wind speed regions are difficult to conduct and the extended fits based on higher wind speed ranges can lead to incorrect estimations. One target of this study was to tackle the challenging measurements at the low wind speed end. The transfer velocites obtained in this study are characterised by low uncertainties and definitely provide a better indication of the low wind speed end gas-exchange behaviour. The results presented here are obtained under slightly stable atmosphere conditions (water temperature lower that the air temperature). No gas exchange due to convection is apparent. In the open ocean, depending on the temperature and the light intensity, convec-

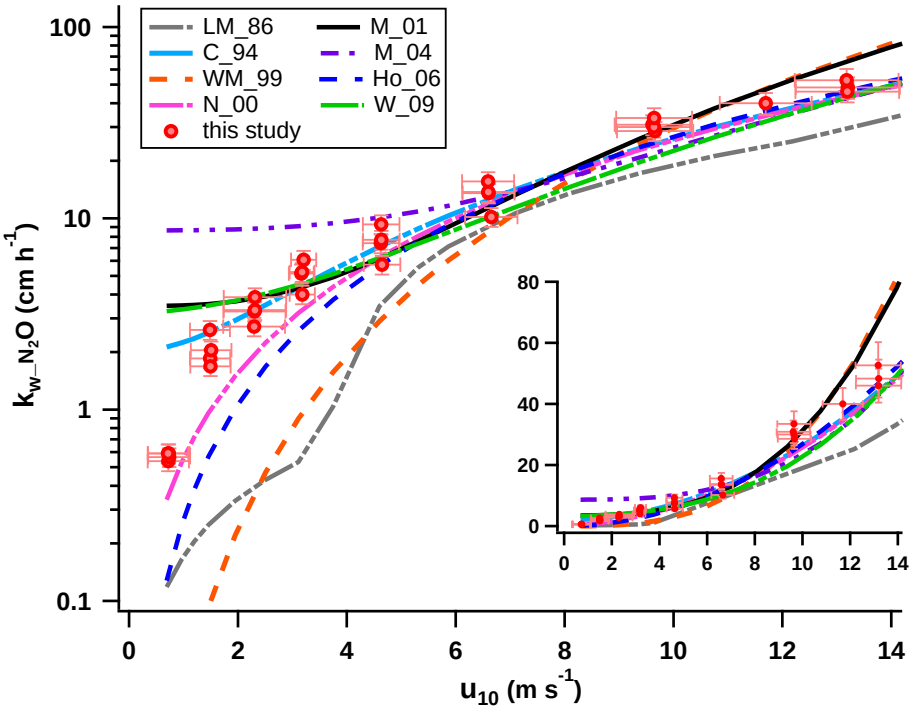

Figure 10. Comparison between the N_2O measurements of this study (red circles) and previous k_w parameterisations. The coloured lines correspond to LM_86: Liss and Merlivat (1986); C_94: Clark et al. (1994); WM_99: Wanninkhof and McGillis (1999); N_00: Nightingale et al. (2000); M_01: McGillis et al. (2001); M_04: McGillis et al. (2004); Ho_06: Ho et al. (2006); and W_09: Wanninkhof et al. (2009).

tion can provoke an increase in the gas exchange which at very low wind speeds is considered significant. Such environmental differences could provide an additional explanation for the huge disagreement observed. The projected absolute quantity differences to the atmospheric budgets, however, are estimated to be small since the fluxes themselves are small. The middle wind speed range seems to be well represented in all studies. At the higher wind speed range, a smaller spread was observed especially above 10 m s^{-1}. This spread, a little more than an order of 2, can lead to great discrepancies in the atmospheric budgets of the related tracers as the corresponding transfer velocities are much larger there.

The transfer velocities obtained in this study, show a closer agreement with the Clark et al. (1994) parameterisation apart from the lowest wind speed. There, our results agree better with Nightingale et al. (2000).

In contrast to the weakly soluble gases, high solubility tracers have received much less attention. In Fig. 11, the total transfer velocity measurements of CH_3OH (here $k_{ta} \sim k_a$) are compared with some available tunnel (Liss, 1973; Mackay and Yeun, 1983, coloured lines) and model (Duce et al., 1991; Jeffery et al., 2010, from COARE Algorithm; Fairall et al., 2003, grey lines) k_a parameterisations as well as a recent CH_3OH field study (Yang, 2013, black line with triangles).

As indicated in Fig. 11, our results agree very well with the previous laboratory parameterisations lying nearer to Mackay and Yeun (1983). Here again the first transfer velocity point deviates, though an increase by the estimated 10 % would still not change this trend. We note that also in the case of k_a, the lower wind speed range of the other experimental studies is covered by a fit extension based on transfer velocities obtained at higher wind speeds.

The transfer velocity values provided by model and field studies are about 1.5 to 2 times lower than the ones derived from the laboratory measurements. This is to be expected as model and field studies include an extra turbulent resistance in the air space at 10 m height.

5 Conclusions

This study has demonstrated that the Aeolotron wind–wave tank in combination with the adopted box model methodology, experimental procedure and instrumentation are capable of generating reliable and reproducible gas transfer velocities for species spanning a wide range of solubilities. The molecules nitrous oxide and methanol have been used to exemplify the behaviour of sparingly soluble and highly soluble species. These represent cases of a water-side and an air-side layer control, as described in Sect. 2. Small differences between the obtained transfer velocity values of the four repetitions of the clean case indicate that various physical parameters should be taken into account in future parameterisations in order to produce better transfer velocity estimations. The

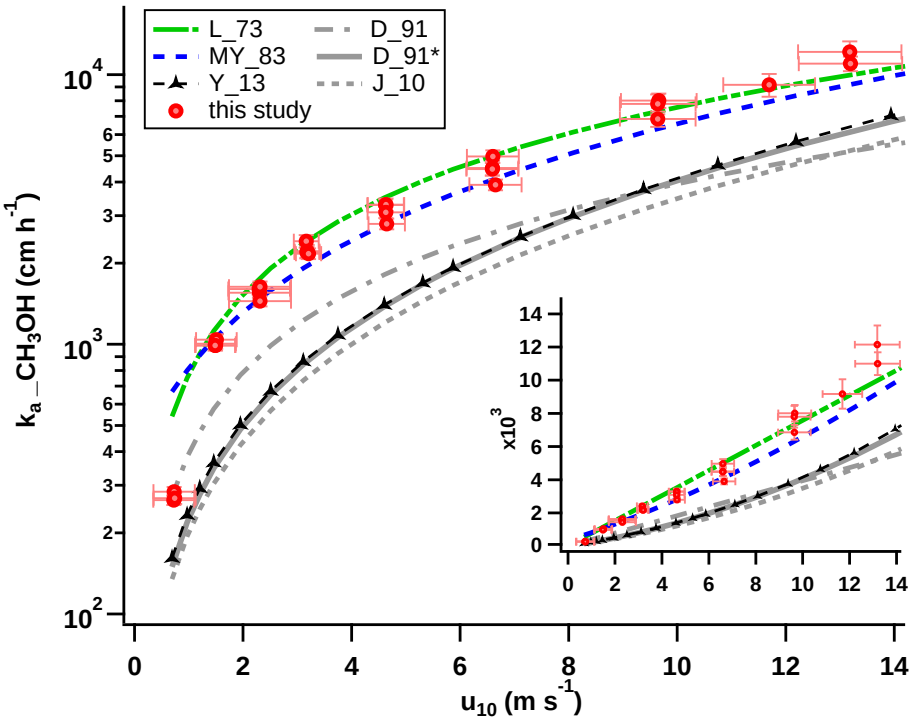

Figure 11. Comparison between the CH_3OH measurements of this study (red circles) and previous k_a parameterisations. Experimental studies are presented with coloured lines: L_73: Liss (1973); MY_83: Mackay and Yeun (1983); and Y_13: Yang (2013), while model studies are given with grey lines: D_91 using the M; D_91* using the Sc_a: Duce et al. (1991); and J_10: Jeffery et al. (2010) using a Smith and Banke (1975) derived drag coefficient term.

complete data set for all species (including the intermediate cases of both layer control) along with the available micro-scale surface property parameters, extending over a low to medium wind speed regime, can be used to generate a generalised parameterisation for the total transfer velocity. The derivation of this expression, which will be invaluable to future modelling efforts, will be presented in a separate publication.

Particularly interesting are the effects on the gas transfer velocity induced by the addition of a surfactant. Despite the surface micro-layer being commonly present on the ocean, its effect on air–sea gas transfer is poorly understood and there is a paucity of data both from the laboratory and the field. The impact of the surfactant is markedly different on the two tracers shown here. A strong reducing effect (up to a factor of 3) was observed for the water-side controlled tracer, N_2O while in the case of CH_3OH, the surfactant showed a quite weaker impact.

We maintain that it is important to monitor the transfer process in both the water-phase (using water-side controlled tracers) and the air-phase layer (using air-side controlled tracers) in order to develop a true enduring and generally applicable model for air–sea gas transfer. The results produced here correspond reasonably well with previous expressions for k_a and k_w. In case of k_w, at low wind speeds there is a wide spread in the literature values, with this study corresponding most closely with those of Clark et al. (1994) and Nightingale et al. (2000). At high wind speeds the previous parameterisations are divided into three groups and this study lies in the central group. Despite the relatively small number of investigations, in case of k_a, the literature spread is much smaller with our results nicely corresponding to the previous laboratory parameterisations (i.e. Liss, 1973; Mackay and Yeun, 1983).

This study, based on data from the world's largest operational annular wind–wave facility, derived from advanced analytical technology which has been set-up to monitor the gas concentration changes in both the air and the water phase simultaneously at unprecedented measurement frequency, has proven to produce high quality transfer velocity measurements. On the basis of our results, we recommend the proposed methodology for future air–water gas-exchange measurements.

Appendix A: Relationship between air-sided and water-sided variables

The experimentally calculated water-sided total transfer velocities, k_{tw}, were converted to the equivalent air-sided total transfer velocities, k_{ta}, using

$$k_{ta} = \alpha k_{tw}. \quad \text{(A1)}$$

Air-sided friction velocities can be converted to water-sided friction velocities by

$$u_{*,w} = \sqrt{\frac{\rho_a}{\rho_w}} u_{*,a}. \quad \text{(A2)}$$

Appendix B: u_{10} derivation using $u_{*,a}$

The wind speed at a height of 10 m, u_{10}, is calculated from its relationship with the air-sided friction velocity and the drag coefficient, C_d, using

$$C_d = \frac{u_{*,a^2}}{u_{10^2}}. \quad \text{(B1)}$$

Here, the Smith and Banke (1975) empirical relationship between the drag coefficient and the wind speed was used

$$10^3 C_d = 0.63 + 0.066 u_{10}. \quad \text{(B2)}$$

Appendix C: Naming conventions

k_w	transfer velocity in water for a water-sided viewer
k_a	transfer velocity in air for an air-sided viewer
k_{tw}	total transfer velocity for a water-sided viewer
k_{ta}	total transfer velocity for an air-sided viewer
c_w	water-side concentration
c_a	air-side concentration
V_w	water volume
V_a	air volume
A	water surface
$\lambda_{f,1}$	leak rate
$\lambda_{f,2}$	flush rate
$\alpha = \frac{c_w}{c_a}$	dimensionless solubility
Sc_w	Schmidt number in water
Sc_a	Schmidt number in air
M	molecular mass
$u_{*,w}$	water-sided friction velocity
$u_{*,a}$	air-sided friction velocity
ρ_w	density of water
ρ_a	density of air
u_{ref}	reference wind speed
σ_s^2	mean square slope
u_{10}	wind speed at 10 m height

Acknowledgements. We own a special thank to J. Auld and T. Klüpfel for their valuable assistance and support during the gas exchage experiments. The mean square slope values were kindly provided by R. Rocholz. R. Sander is thanked for the helpful and insightful discussions on solubility matters considering this manuscript. Furthermore, we thank all members of B. Jähne's group for their understanding and support during the measurements. We acknowledge the financial support of the BMBF Verbundprojekt SOPRAN (www.sopran.pangaea.de; SOPRAN grant 03F0611A, 03F0611K, 03F0611F and 03F0662F)

The service charges for this open access publication have been covered by the Max Planck Society.

Edited by: J. Shutler

References

Benkelberg, H. J., Hamm, S., and Warneck, P.: Henry's law coefficients for aqueous solutions of acetone, acetaldehyde and acetonitrile, and equilibrium constants for the addition compounds of acetone and acetaldehyde with bisulfite, J. Atmos. Chem., 20, 17–34, doi:10.1007/Bf01099916, 1995.

Betterton, E. A. and Hoffmann, R. M.: Henry's law constants of some environmentally important aldehydes., Environ. Sci. Technol., 22, 1415–1418, doi:10.1021/Es00177a004, 1988.

Bopp, M.: Luft und wasserseitige Strömungsverhältnisse im ringförmigen Heidelberger Wind-Wellen-Kanal (Aeolotron), Master Thesis, University of Heidelberg, available at: http://www.ub.uni-heidelberg.de/archiv/16962 (last access: 18 June 2014), 2014.

Broecker, W. S., Peng, T. H., Ostlund, G., and Stuiver, M.: The Distribution of Bomb Radiocarbon in the Ocean, J. Geophys. Res.-Oceans, 90, 6953–6970, doi:10.1029/Jc090ic04p06953, 1985.

Carpenter, L. J., Archer, S. D., and Beale, R.: Ocean-atmosphere trace gas exchange, Chem. Soc. Rev., 41, 6473–6506, 2012.

Clark, J. F., Wanninkhof, R., Schlosser, P., and Simpson, H. J.: Gas-Exchange Rates in the Tidal Hudson River Using a Dual Tracer Technique, Tellus B, 46, 274–285, 1994.

Cosovic, B. and Vojvodic, V.: Voltammetric analysis of surface active substances in natural seawater, Electroanalysis, 10, 429–434, doi:10.1002/(SICI)1521-4109(199805)10:6<429::AID-ELAN429>3.0.CO;2-7, 1998.

Dacey, J. W. H., Wakeham, G. S., and Howes, L. B.: Henry's law constants for dimethylsulfide in freshwater and seawater, Geophys. Res. Lett., 11, 991–994, doi:10.1029/Gl011i010p00991, 1984.

Danckwerts, P. V.: Significance of Liquid-Film Coefficients in Gas Absorption, Ind. Eng. Chem., 43, 1460–1467, 1951.

Donelan, M. A. and Wanninkhof, R.: Concepts and Issues, in: Gas Transfer at Water Surfaces (127), American Geophysical Union, edited by: Donelan, M. A., Drennan, W. M., Saltzman, E. S., and Wanninkhof, R., 1–10, 2002.

Duce, R. A., Liss, P. S., Merrill, J. T., Atlas, E. L., Buat-Menard, P., Hicks, B. B., Miller, J. M., Prospero, J. M., Arimoto, R., Church, T. M., Ellis, W., Galloway, J. N., Hansen, L., Jickells, T. D., Knap, A. H., Reinhardt, K. H., Schneider, B., Soudine, A., Tokos, J. J., Tsunogai, S., Wollast, R., and Zhou, M.: The atmospheric input of trace species to the world ocean, Geophys. Res. Lett., 5, 193–259, doi:10.1029/91GB01778, 1991.

Fairall, C. W., Bradley, E. F., Hare, J. E., Grachev, A. A., and Edson, J. B.: Bulk Parameterization of Air–Sea Fluxes: Updates and Verification for the COARE Algorithm, J. Climate, 16, 571–591, doi:10.1175/1520-0442(2003)016<0571:BPOASF>2.0.CO;2, 2003.

Field, C. B., Behrenfeld, M. J., Randerson, J. T., and Falkowski P.: Primary production of the biosphere, Science, 281, 237–240, 1998.

Frew, N. M., Goldman, J. C., Denett, M. R., and Johnson, A. S.: Impact of phytoplankton-generated surfactants on air-sea gas exchange, J. Geophys. Res.-Oceans, 95, 3337–3352, doi:10.1029/JC095iC03p03337, 1990.

Frew, N. M., Bock, E. J., McGillis, W. R., Karachintsev, A. V., Hara, T., Münsterer, T., and Jähne, B.: Variation of air-water gas transfer with wind stress and surface viscoelasticity, in: Air-water Gas Transfer, Selected Papers from the Third International Symposium on Air-Water Gas Transfer, edited by: Jähne, B. and Monahan, E. C., Aeon, Hanau, 529–541, 1995.

Griffiths, P. R.: Fourier Transform Infrared Spectrometry, Wiley Interscience, 2nd Edn., 2007.

Ho, D. T., Law, C. S., Smith, M. J., Schlosser, P., Harvey, M., and Hill, P.: Measurements of air-sea gas exchange at high wind speeds in the Southern Ocean: Implications for global parameterizations, Geophys. Res. Lett., 33, L16611, doi:10.1029/2006GL026817, 2006.

Jähne, B.: Air-sea gas exchange, in: Encyclopedia Ocean Sciences, Elsevier, 3434–3444, 2009.

Jähne, B. and Haußecker, H.: Air-water gas exchange, Annu. Rev. Fluid Mech., 30, 443–468, 1998.

Jähne, B., Münnich, K. O., and Siegenthaler, U.: Measurements of Gas-Exchange and Momentum-Transfer in a Circular Wind-Water Tunnel, Tellus, 31, 321–329, 1979.

Jähne, B., Münnich, K. O., Bösinger, R., Dutzi, A., Huber, W., and Libner, P.: On the Parameters Influencing Air-Water Gas-Exchange, J. Geophys. Res.-Oceans, 92, 1937–1949, 1987.

Janini, G. M. and Quaddora, A. L.: Determination of activity coefficients of oxygenated hydrocarbons by liquid-liquid chromatography, J. Liq. Chromatogr., 9, 39–53, doi:10.1080/01483918608076621, 1986.

Jeffery, C. D., Robinson, I. S., and Woolf, D. K.: Tuning a physically-based model of the air-sea gas transfer velocity, Ocean Model., 31, 28–35, doi:10.1016/j.ocemod.2009.09.001, 2010.

Krall, K. E.: Laboratory Investigations of Air-Sea Gas Transfer under a Wide Range of Water Surface Conditions, Dissertation, University of Heidelberg, available at: http://www.ub.uni-heidelberg.de/archiv/14392 (last access: 18 June 2014), 2013.

Krall, K. E. and Jähne, B.: First laboratory study of air-sea gas exchange at hurricane wind speeds, Ocean Sci., 10, 257–265, doi:10.5194/os-10-257-2014, 2014.

Kräuter, C.: Aufteilung des Transferwiderstandes zwischen Luft und Wasser beim Austausch flüchtiger Substanzen mittlerer Löslichkeit zwischen Ozean und Atmosphäre, Diploma, University of Heidelberg, Germany, available at: http://www.ub.

uni-heidelberg.de/archiv/13010 (last access: 18 June 2014), 2011.

Lindinger, W., Hansel, A., and Jordan, A.: On-line monitoring of volatile organic compounds at pptv levels by means of proton-transfer-reaction mass spectrometry (PTR-MS) – Medical applications, food control and environmental research, Int. J. Mass. Spectrom., 173, 191–241, doi:10.1016/S0168-1176(97)00281-4, 1998.

Liss, P. S.: Processes of Gas-Exchange across an Air-Water Interface, Deep-Sea Res., 20, 221–238, 1973.

Liss, P. S. and Merlivat, L.: Air-sea gas exchange rates: Introduction and synthesis, in The role of air-sea exchange in geochemical cycling, Reidel, Boston, MA, 113–129, 1986.

Liss, P. S. and Slater, P. G.: Flux of Gases across Air-Sea Interface, Nature, 247, 181–184, 1974.

Mackay, D. and Yeun, A. T. K.: Mass-Transfer Coefficient Correlations for Volatilization of Organic Solutes from Water, Environ. Sci. Tech., 17, 211–217, doi:10.1021/Es00110a006, 1983.

McGillis, W. R., Edson, J. B., Ware, J. D., Dacey, J. W. H., Hare, J. E., Fairall, C. W., and Wanninkhof, R.: Carbon dioxide flux techniques performed during GasEx-98, Mar. Chem., 75, 267–280, doi:10.1016/S0304-4203(01)00042-1, 2001.

McGillis, W. R., Edson, J. B., Zappa, C. J., Ware, J. D., McKenna, S. P., Terray, E. A., Hare, J. E., Fairall, C. W., Drennan, W., Donelan, M., DeGrandpre, M. D., Wanninkhof, R., and Feely, R. A.: Air-sea CO_2 exchange in the equatorial Pacific, J. Geophys. Res.-Oceans, 109, C08S02, doi:10.1029/2003jc002256, 2004.

Millet, D. B., Jacob, D. J., Custer, T. G., de Gouw, J. A., Goldstein, A. H., Karl, T., Singh, H. B., Sive, B. C., Talbot, R. W., Warneke, C., and Williams, J.: New constraints on terrestrial and oceanic sources of atmospheric methanol, Atmos. Chem. Phys., 8, 6887–6905, doi:10.5194/acp-8-6887-2008, 2008.

Millet, D. B., Guenther, A., Siegel, D. A., Nelson, N. B., Singh, H. B., de Gouw, J. A., Warneke, C., Williams, J., Eerdekens, G., Sinha, V., Karl, T., Flocke, F., Apel, E., Riemer, D. D., Palmer, P. I., and Barkley, M.: Global atmospheric budget of acetaldehyde: 3-D model analysis and constraints from in-situ and satellite observations, Atmos. Chem. Phys., 10, 3405–3425, doi:10.5194/acp-10-3405-2010, 2010.

Nielsen, R.: Gasaustausch – Entwicklung und Ergebnis eines schnellen Massenbilanzverfahrens zur Messung der Austauschparameter, Dissertation, University of Heidelberg, available at: http://www.ub.uni-heidelberg.de/archiv/5032 (last access: 18 June 2014), 2004.

Nightingale, P. D.: Air-sea gas exchange. Lower Atmosphere Processes, in: Surface Ocean, AGU Books Board, edited by: Le Quéré, C. and Saltzman, E. S., 69–97, 2009.

Nightingale, P. D., Malin, G., Law, C. S., Watson, A. J., Liss, P. S., Liddicoat, M. I., Boutin, J., and Upstill-Goddard, R. C.: In situ evaluation of air-sea gas exchange parameterization using novel conservation and volatile tracers, Global Biogeochem. Cy., 14, 373–387, 2000.

Pozzer, A., Jöckel, P., Sander, R., Williams, J., Ganzeveld, L., and Lelieveld, J.: Technical Note: The MESSy-submodel AIRSEA calculating the air-sea exchange of chemical species, Atmos. Chem. Phys., 6, 5435–5444, doi:10.5194/acp-6-5435-2006, 2006.

Robbins, G. A., Wang, V., and Stuart, D. J.: Using the headspace method to determine Henry's law constants, Anal. Chem., 65, 3113–3118, doi:10.1021/Ac00069a026, 1993.

Rocholz, R.: Spatiotemporal Measurement of Short Wind-Driven Water Waves, Dissertation, University of Heidelberg, available at: http://www.ub.uni-heidelberg.de/archiv/8897 (last access: 18 June 2014), 2008.

Salter, M. E., Upstill-Goddard, R. C., Nightingale, P. D., Archer, S. D., Blomquist, B., Ho, D. T., Huebert, B., Schlosser, P., and Yang, M.: Impact of an artificial surfactant release on air–sea gas fluxes during Deep Ocean Gas Exchange Experiment II, J. Geophys. Res., 116, C11016, doi:10.1029/2011JC007023, 2011.

Saltzman, E.: Introduction to Surface Ocean–Lower Atmosphere Processes, in: Surface Ocean-Lower Atmosphere Processes, Geophysical Research Series, 187, 2009.

Sander, R.: Compilation of Henry's Law Constants for Inorganic and Organic Species of Potential Importance in Environmental Chemistry (Version 3), available at: http://www.henrys-law.org (last access: 18 June 2014), 1999.

Schaffer, D. L. and Daubert, E. T.: Gas-liquid chromatographic determination of solution properties of oxygenated compounds in water, Anal. Chem., 286, 1585–1589, 1969.

Smith, S. D. and Banke, E. G.: Variation of Sea-Surface Drag Coefficient with Wind Speed, Q. J. Roy. Meteorol. Soc., 101, 665–673, 1975.

Snider, J. R. and Dawson, A. G.: Tropospheric light alcohols, carbonyls, and acetonitrile: Concentrations in the southwestern United States and Henry's law data, J. Geophys. Res., 90D, 3797–3805, doi:10.1029/Jd090id02p03797, 1985.

Wanninkhof, R. and McGillis, W. R.: A cubic relationship between air-sea CO_2 exchange and wind speed, Geophys. Res. Lett., 26, 1889–1892, doi:10.1029/1999gl900363, 1999.

Wanninkhof, R., Asher, W., Weppernig, R., Chen, H., Schlosser, P., Langdon, C., and Sambrotto, R.: Gas Transfer Experiment on Georges Bank Using 2 Volatile Deliberate Tracers, J. Geophys. Res.-Oceans, 98, 20237–20248, 1993.

Wanninkhof, R., Asher, W. E., Ho, D. T., Sweeney, C., and McGillis, W. R.: Advances in quantifying air-sea gas exchange and environmental forcing, Annu. Rev. Mar. Sci., 1, 213–244, 2009.

Watson, A. J., Upstill-Goddard, R. C., and Liss, P. S.: Air Sea Gas-Exchange in Rough and Stormy Seas Measured by a Dual-Tracer Technique, Nature, 349, 145–147, 1991.

Weiss, R. F. and Price, B. A.: Nitrous oxide solubility in water and seawater, Mar. Chem., 8, 347–359, doi:10.1016/0304-4203(80)90024-9, 1980.

Williams, J., Holzinger, R., Gros, V., Xu, X., Atlas, E., and Wallace, D. W. R.: Measurements of organic species in air and seawater from the tropical Atlantic, Geophys. Res. Lett., 31, L23S06, doi:10.1029/2004GL020012, 2004.

Wurl, O., Wurl, E., Miller, L., Johnson, K., and Vagle, S.: Formation and global distribution of sea-surface microlayers, Biogeosciences, 8, 121–135, doi:10.5194/bg-8-121-2011, 2011.

Yang, M., Nightingale, P. D., Beale, R., Liss, P. S., Blomquist, B., and Fairall, C.: Atmospheric deposition of methanol over the Atlantic Ocean, P. Natl. Acad. Sci. USA, 110, 20034–20039, doi:10.1073/pnas.1317840110, 2013.

Yaws, C. L.: Handbook of Transport Property Data, Gulf Publishing Company, 1995.
Yaws, C. L. and Pan, X.: Liquid Heat-Capacity for 300 Organics, Chem. Eng., 99, 130–134, 1992.
Zappa, C. J., Asher, W. E., Jessup, A. T., Klinke, J., and Long, S. R.: Microbreaking and the enhancement of air-water transfer velocity, J. Geophys. Res.-Oceans, 109, C08S16, doi:10.1029/2003jc001897, 2004.